行政院國家科學委員會專題研究計畫　成果報告

長矩形微流道不可壓縮層流與紊流場之三維數值計算

計畫類別：個別型計畫
計畫編號：NSC94-2212-E-032-007-
執行期間：94 年 08 月 01 日至 95 年 07 月 31 日
執行單位：淡江大學航空太空工程學系

計畫主持人：陳慶祥

報告類型：精簡報告

處理方式：本計畫可公開查詢

中　華　民　國 95 年 9 月 19 日

長矩形微流道不可壓縮層流與紊流場之三維數值計算

Three-Dimensional Numerical Simulation of Incompressible Laminar and Turbulent Flows in Long Microchannels

中文摘要

本文的目的是研究溫度效應對長微流道不可壓縮流摩擦特性的影響，水的物理特性如黏滯係數等隨著溫度的改變量很大，這些係數的改變使得長微流道內的溫度、壓力及雷諾數的分佈變得非線性化。因此分析此類流場時必須將溫度效應包括進來。而本研究利用簡化的 Navier-Stokes 方程式，來計算長微流道裡的摩擦特性。本數值計算的優點，在於它的統御方程式是一個具有拋物線型特性的方程式，在求解速度上至少比完全 Navier-Stokes 方程式快上百倍到千倍。而此一快速而準確的研究工具可幫助我們詳細的研究此類問題。

關鍵字 ： 微流道，摩擦，數值分析

Abstract

The objective of this research is to investigate numerically the effect of temperature on friction characteristics of incompressible flow in long microchannels. The physical properties of water change significantly with temperature. These property changes result in highly nonlinear temperature, pressure, and Reynolds number distributions along the microchannel axis. These temperature effects must be taken into account to accurately predict the friction characteristics of incompressible microchannel flows. The major advantage of the present numerical procedure is its fast speed due to the parabolic character of the governing equations. It is at least two to three orders of magnitude faster than the full Navier-Stokes simulation. The present numerical procedure can be a fast and accurate tool in studying long microchannels flows.

Keywords：microchannel flow, friction, numerical analysis

1 INTRODUCTION

Micro-electronic-mechanical systems (MEMS) are becoming a rapidly developing research field. A large number of recent investigations study the fundamentals of microchannel flow. This is because these channels have potential applications in diverse areas such as microelectronics, biological cell reactors, biological chips, and micro heat exchangers, etc. The experimental results available in the literature show that the friction and heat transfer characteristics of fluid flow in

micro devices differ from those in macroscopic devices.

The experimental investigations related to the pressure drop in microchannels are introduced first. Wu and Little [1, 2] conducted tests on rectangular microchannels with hydraulic diameters ranged from 50 to 80 μm. Their results indicated an earlier transition from laminar to turbulent flow region. Their measured $f \cdot \mathrm{Re}$ value for laminar flows was constant but was much higher than 64. The measured friction factor for turbulent flows was also much higher when compared with the conventional results.

Choi et al. [3, 4] measured friction factor for both laminar and turbulent flows in microtubes. The internal diameters of these microtubes ranged from 3 to 81 μm and the working fluid was nitrogen gas. They found that the measured $f \cdot \mathrm{Re}$ values were about 53 for laminar flows, instead of 64 as predicted by the incompressible flow theory. The measured friction factor for turbulent flows was also smaller than that predicted using conventional correlations for larger tubes. Yu [5] investigated the fluid flow and heat transfer characteristics of nitrogen gas and water in microtubes with diameters of 19, 52 and 102 μm. They reported that the measured friction factors were about the same as that predicted by the Blasius correlation.

Chen et al. [6] solved the Navier-Stokes equations to simulate two-dimensionally gaseous flow in microchannels. They confirmed that for very small Reynolds numbers, on the order of 10^{-3}, the fluid in a microchannel is indeed isothermal due to the extraordinarily large momentum and heat diffusion in the smallest dimension direction. But if the Reynolds number is large, the isothermal flow assumption is no longer valid. Chen et al. [7] solved the compressible boundary-layer equations to simulate compressible flow in microtubes. The numerical results compared well with the experimental data. They reported that slip and compressibility effects are the two major factors that cause difference in flow behavior in conventional and micro tubes

Sobhan and Garimella [8] conducted a comparative study of the experimental results and theoretical investigations available in the literature on fluid flow and heat transfer in microchannels. They reported that there is little agreement between the experimental results reported by different investigators. Also, the information in the literature does not point to unequivocal trends of variation or reasons of such trends. They concluded that a reliable prediction of heat transfer and pressure drop in microchannels is not possible and additional studies are necessary.

The major advantage of the present numerical procedure is its fast speed due to the parabolic character of the governing equations. An efficient space marching algorithm is adopted to solve the governing equations. It is at least two to three orders of magnitude faster than the full Navier-Stokes simulation. This is because the unsteady Navier-Stokes equations are a mixed set of hyperbolic-parabolic equations that are integrated in time until a steady state solution is reached. This procedure is inefficient because of its time marching procedure. The present numerical procedure

is as accurate as the full Navier-Stokes simulation except very near the entrance region. But this region is small due to the large channel length to hydraulic diameter ratio in microchannel flows. The present numerical procedure is a fast and accurate tool in studying steady incompressible microchannel flows.

2 GOVERNING EQUATIONS

The flow is assumed to be governed by the reduced form of the steady three-dimensional incompressible laminar Navier-Stokes equations [10]. The reduced equations cannot model the entrance region accurately, but this region is small for the long microchannels studied in this work. Water is used as the working fluid for the present work. Fig. 1 depicts the geometry and coordinate system of a rectangular microchannel. The non-dimensional governing equations are given below [10].

The continuity equation

$$\frac{\partial(\tilde{\rho}\tilde{u})}{\partial\tilde{x}}+\frac{\partial(\tilde{\rho}\tilde{v})}{\partial\tilde{y}}+\frac{\partial(\tilde{\rho}\tilde{w})}{\partial\tilde{z}}=0 \tag{1}$$

The momentum equations

$$\begin{aligned}&\tilde{\rho}[\tilde{u}\frac{\partial\tilde{u}}{\partial\tilde{x}}+\tilde{v}\frac{\partial\tilde{u}}{\partial\tilde{y}}+\tilde{w}\frac{\partial\tilde{u}}{\partial\tilde{z}}]\\&=-\frac{d\tilde{p}_m}{d\tilde{x}}+\frac{1}{\mathrm{Re}}\frac{\partial}{\partial\tilde{y}}(\tilde{\mu}\frac{\partial\tilde{u}}{\partial\tilde{y}})+\frac{1}{\mathrm{Re}}\frac{\partial}{\partial\tilde{z}}(\tilde{\mu}\frac{\partial\tilde{u}}{\partial\tilde{z}})\end{aligned} \tag{2}$$

$$\begin{aligned}&\tilde{\rho}(\tilde{u}\frac{\partial\tilde{v}}{\partial\tilde{x}}+\tilde{v}\frac{\partial\tilde{v}}{\partial\tilde{y}}+\tilde{w}\frac{\partial\tilde{v}}{\partial\tilde{z}})=-\frac{\partial\tilde{p}_c}{\partial\tilde{y}}+\frac{4}{3\cdot\mathrm{Re}}\frac{\partial}{\partial\tilde{y}}(\tilde{\mu}\frac{\partial\tilde{v}}{\partial\tilde{y}})\\&+\frac{1}{\mathrm{Re}}\frac{\partial}{\partial\tilde{z}}(\tilde{\mu}\frac{\partial\tilde{v}}{\partial\tilde{z}})+\frac{1}{3\cdot\mathrm{Re}}\frac{\partial}{\partial\tilde{z}}(\tilde{\mu}\frac{\partial\tilde{w}}{\partial\tilde{y}})\end{aligned} \tag{3}$$

$$\begin{aligned}&\tilde{\rho}(\tilde{u}\frac{\partial\tilde{w}}{\partial\tilde{x}}+\tilde{v}\frac{\partial\tilde{w}}{\partial\tilde{y}}+\tilde{w}\frac{\partial\tilde{w}}{\partial\tilde{z}})=-\frac{\partial\tilde{p}_c}{\partial\tilde{z}}+\frac{1}{3\cdot\mathrm{Re}}\frac{\partial}{\partial\tilde{y}}(\tilde{\mu}\frac{\partial\tilde{v}}{\partial\tilde{z}})\\&+\frac{1}{\mathrm{Re}}\frac{\partial}{\partial\tilde{y}}(\tilde{\mu}\frac{\partial\tilde{w}}{\partial\tilde{y}})+\frac{4}{3\cdot\mathrm{Re}}\frac{\partial}{\partial\tilde{z}}(\tilde{\mu}\frac{\partial\tilde{w}}{\partial\tilde{z}})\end{aligned} \tag{4}$$

The energy equation

$$\begin{aligned}&\tilde{\rho}(\tilde{u}\frac{\partial\tilde{T}}{\partial\tilde{x}}+\tilde{v}\frac{\partial\tilde{T}}{\partial\tilde{y}}+\tilde{w}\frac{\partial\tilde{T}}{\partial\tilde{z}})\\&=(\tilde{u}\frac{\partial\tilde{p}_m}{\partial\tilde{x}})+\frac{1}{\mathrm{Re}\cdot\mathrm{Pr}}[\frac{\partial}{\partial\tilde{y}}(\tilde{k}\frac{\partial\tilde{T}}{\partial\tilde{y}})+\frac{\partial}{\partial\tilde{z}}(\tilde{k}\frac{\partial\tilde{T}}{\partial\tilde{z}})]\\&+\frac{1}{\mathrm{Re}_{in}}[\tilde{\mu}(\frac{\partial\tilde{u}}{\partial\tilde{y}})^2+\tilde{\mu}(\frac{\partial\tilde{u}}{\partial\tilde{z}})^2]\end{aligned} \tag{5}$$

The integral constraint on mass flow through the channel

$$\int_{-H/2D}^{H/2D}\int_{-W/2D}^{W/2D}\tilde{\rho}\,\tilde{u}\;d\tilde{y}\,d\tilde{z}=\dot{\tilde{m}} \tag{6}$$

The above equations are normalized by the following inlet values,

$$\tilde{u} = \frac{u}{u_{in}};\quad \tilde{v} = \frac{v}{u_{in}};\quad \tilde{w} = \frac{w}{u_{in}};\quad \tilde{\rho} = \frac{\rho}{\rho_{in}};\tilde{T} = \frac{T}{T_{in}},$$

$$\tilde{x} = \frac{x}{D};\quad \tilde{y} = \frac{y}{D};\quad \tilde{z} = \frac{z}{D};D = \frac{2 \cdot W \cdot H}{W + H}$$

$$\tilde{p} = \frac{p}{\rho_{in} u_{in}^2};\quad \mathrm{Re} = \frac{\rho_{in} u_{in} D}{\mu_{in}};\quad \tilde{\mu} = \frac{\mu}{\mu_{in}},\quad \tilde{k} = \frac{k}{k_{in}}$$

$$c_p = \frac{\gamma \cdot R}{\gamma - 1};\quad \mathrm{Pr} = \frac{c_p \cdot \mu_{in}}{k_{in}}.$$

The dynamic viscosity μ and thermal conductivity k are functions of temperature and are described by

$$k = a_0 + a_1 T + a_2 T^2 \tag{7}$$

$$\mu = b_0\, 10^{b_1/(T - b_2)} \tag{8}$$

The constants for the above two equations are listed in Table 1. In the reduced Navier-Stokes equations described above we neglect the diffusion terms in the $\tilde{x}$-direction. This is reasonable, because the momentum and energy diffusions in the $\tilde{x}$-direction are much smaller than that in the $\tilde{y}$- and $\tilde{z}$-directions for the long microchannel flows studied in this paper. The pressure $\tilde{p}_m$ in the $\tilde{x}$-momentum equation is different from the pressure $\tilde{p}_c$ in the $\tilde{y}$- and $\tilde{z}$-momentum equations. The pressures $\tilde{p}_m$ and $\tilde{p}_c$ are calculated separately. The pressure $\tilde{p}_m$ is a space-averaged pressure over a $\tilde{y}$ - $\tilde{z}$ cross-section. The gradient $d\tilde{p}_m / d\tilde{x}$ is calculated iteratively in a $\tilde{y}$ - $\tilde{z}$ cross-section by satisfying the global mass conservation. The pressure $\tilde{p}_c$ is a correction to the pressure $\tilde{p}_m$. It only influences the $\tilde{v}$- and $\tilde{w}$-velocities; it does not affect the $\tilde{u}$-velocity. The three momentum equations and the continuity equation are combined to construct a Poisson equation to solve for $\tilde{p}_c$ in a $\tilde{y} - \tilde{z}$ plane.

The velocity and temperature boundary conditions are

$u_w = \mathrm{v}_w = w_w = 0$ at the walls

$$q_w = -K \frac{\partial T}{\partial n} = 500 \frac{watts}{m^2}$$

for the uniform wall heat flux boundary condition

$T_w = 340K$

for the isothermal wall boundary condition

$T_{in} = 290K$

for the fluid temperature at the channel inlet

The dimensions, inlet and outlet conditions, and boundary conditions for the microchannels simulated in this study are listed in Table 1. In the numerical

simulations the channel width and height were varied to study the effect of aspect ratio. The channel height *H* was calculated by $H = \sqrt{AREA/AR}$. *AREA* is the channel cross-sectional area. *AR* is the channel aspect ratio and is defined by *channel width/channel height.* The channel width *W* was calculated by $H \times AR$. The channel length was 1000 times the hydraulic diameter. The working fluid was water. The channel outlet pressure was fixed at the atmospheric pressure. The pressure ratio was defined as $PR \equiv inlet\ \ pressure / outlet\ \ pressure$. The above definitions were used in all the simulations in this paper.

3 NUMERICAL PROCEDURES

The reduced Navier-Stokes equations are a set of parabolic equations in the $\tilde{x}$ -direction. They are solved using an efficient space marching procedure [9]. The procedure is described below.

(1) The $\tilde{u}^{i+1}$ velocity is computed from the $\tilde{x}$ -momentum equation, Eq. (2). The inlet pressure, inlet temperature, and a guessed mass flow rate are given as the initial conditions for the $\tilde{x}$ -momentum equation. The pressure gradient at each $\tilde{x}$ -station is iterated until the global mass constraint, Eq. (6), is satisfied [10]. The Newton-Raphson method [10] is employed to update the pressure gradient.

$$\left(\frac{d\tilde{p}_m}{d\tilde{x}}\right)_{n+1} = \left(\frac{d\tilde{p}_m}{d\tilde{x}}\right)_n - \frac{\dot{\tilde{m}}_n}{\dot{\tilde{m}}_n - \dot{\tilde{m}}_{n-1}} \cdot \left[\left(\frac{d\tilde{p}_m}{d\tilde{x}}\right)_n - \left(\frac{d\tilde{p}_m}{d\tilde{x}}\right)_{n-1}\right] \qquad (9)$$

The mass flow rate $\dot{\tilde{m}}$ is a function of the pressure gradient. Two initial guesses are required before using the above equation.

(2) The pressure correction $\tilde{p}_c$ at each cross-section is computed from the Poisson equation.

(3) The pressure correction $\tilde{p}_c$ obtained from step (2) is substituted into the $\tilde{y}$ - and $\tilde{z}$ -momentum equations, Eqs. (3) and (4), to solve for the $\tilde{v}^{i+1}$ and $\tilde{w}^{i+1}$ velocities.

(4) The temperature $\tilde{T}^{i+1}$ is computed from the energy equation, Eq. (5).

(5) Steps 1 to 5 complete the calculation at a $\tilde{y} - \tilde{z}$ cross-section. The solution then marches along the channel axis to the channel outlet. The outlet pressure is assumed to be atmospheric pressure and is specified at the beginning of a simulation. If the calculated outlet pressure is less than atmospheric pressure, then the guessed mass flow rate is too large. If the calculated outlet pressure is greater than atmospheric pressure, then the guessed mass flow rate is too small. The program then goes back to step 1 with an updated mass flow rate. The Newton-Raphson method [10] is used to

update the mass flow rate,

$$\dot{\tilde{m}}_{k+1} = \dot{\tilde{m}}_k - \frac{\Delta\tilde{p}_m{}^k}{\Delta\tilde{p}_m{}^k - \Delta\tilde{p}_m{}^{k-1}} \cdot \left(\dot{\tilde{m}}_k - \dot{\tilde{m}}_{k-1} \right) \tag{10}$$

In the above equation *k* is the global iteration number. Marching the solution from the channel inlet to outlet is one global-iteration. The parameter $\Delta\tilde{p}_m$ is defined by $\Delta\tilde{p}_m = \tilde{p}_{atm} - \tilde{p}^k_{m,\,out}$, $\tilde{p}_{atm}$ is non-dimensional atmospheric pressure and $\tilde{p}^k_{m,\,out}$ is the numerically calculated channel outlet pressure at the k-th global-iteration.

4 RESULTS AND DISCUSSION

In order to validate the numerical program, the program was first used to calculate the friction factor for the flow in conventional-size channels. The channel height was fixed at 1cm. The channel width was varied to obtain different aspect ratios. The channel length was 1000 times the hydraulic diameter. The working fluid was water. The channel outlet pressure was atmospheric pressure and the pressure ratio, $PR \equiv inlet\ pressure / outlet\ pressure$, was 1.001. Several different aspect ratios were simulated. The simulated conditions are listed in Table 1. The calculated $f \cdot \mathrm{Re}$ values are listed in Table 2. The parameter Re in Table 2 was defined by $\mathrm{Re} = \dot{m} D/(\mu W H)$. Also listed in Table 2 for comparison are the results of two dimensional numerical simulations conducted by Shaw and London [11]. In Shaw and London's report $f \cdot \mathrm{Re}$ is a function of aspect ratio, $AR \equiv channel\ height / channel\ width$, and is independent of Reynolds number. As demonstrated in Table 2, the agreement between the present numerical solution and Shaw and London's results is excellent. The difference is less than 0.2%. This close agreement validated our numerical program.

Water is the most often used liquid in cooling equipment. Yet, its physical properties change remarkably with changing temperature. For example, its conductivity increases from about $0.56\,w/(m \cdot K)$ at 273K to about $0.68\,w/(m \cdot K)$ at 373K, a 21% increase. Its absolute viscosity decreases from about $1.76 \times 10^{-3}\,N \cdot s/m^2$ at 273K to about $0.28 \times 10^{-3}\,N \cdot s/m^2$ at 373K, an 84% decrease. These property changes affect the friction and heat transfer characteristics of microchannel flows significantly. To investigate these effects we simulated microchannel flows subject to changing fluid properties. The simulated conditions are listed in Table 3.

Figure 2 depicts the pressure distributions along the channel axis for microchannel flows subject to the isothermal wall condition. The inlet water temperature was 290K and the wall temperature was 340K as listed in Table 3. The

pressure ratios, PR, simulated were 2, 4, and 6. The pressure distribution is nonlinear for PR=6 case. This is because the fluid properties, especially viscosity, change significantly with changing temperature. Near the channel inlet the mean temperature is lower, the viscosity is larger, so that the wall shear stress is also higher, and this results in a larger pressure drop. Near the channel outlet the mean temperature is higher, the viscosity is lower, so that the wall shear stress is also lower, and this results in a smaller pressure drop. The pressure drop therefore is of concave shape. The pressure distribution for PR=2 case is nearly linear. This is because the pressure ratio is small and this results in a smaller fluid velocity. Therefore, the fluid gets heat much faster from the wall. The fluid temperature reaches the wall temperature fairly quickly and its properties become constant.

Figure 3 depicts the $f \cdot \mathrm{Re}$ distributions along the channel axis for microchannel flows of Fig. 2. The local friction factor was calculated from $f_{local} = \frac{8\tau_w}{\rho_m u_m}$. The symbol τ_w is the local wall shear stress. The symbols ρ_m and u_m are the average density and velocity over a cross-section, respectively. The $f \cdot \mathrm{Re}$ value reaches a constant value, 56.90, for PR=2, 4, and 6 cases. This value is the same as that predicted by Shaw and London [11] for two-dimensional channel flow with constant properties. But its variation along the microchannel axis actually is quite nonlinear. This result demonstrates that the conventional two-dimensional results cannot be used for microchannel flows. Property changes must be taken into account for microchannel flows with significant temperature changes.

Figure 4 depicts the pressure distributions along the channel axis for microchannel flows subject to the constant heat flux condition. The inlet water temperature was 290K and PR=6 as listed in Table 3. Three heat flux conditions, Q=12000, 120000, 280000 w/m^2, were simulated. The pressure distribution is quite nonlinear for the Q=280000 case, due to its large fluid temperature change. The fluid temperature at the outlet reaches 370K.

Figure 5 depicts the $f \cdot \mathrm{Re}$ distributions along the channel axis for microchannel flows of Fig. 4. Unlike the results of Fig. 3, the $f \cdot \mathrm{Re}$ value does not reach a constant value for different heat flux conditions. The $f \cdot \mathrm{Re}$ value of the Q=12000 case is nearly constant, 56.40, due to the small heat input. This value is also very close to that predicted by Shaw and London's two-dimensional calculation [11]. The $f \cdot \mathrm{Re}$ distribution becomes quite nonlinear for the other two higher heat flux conditions. There is no constant value reached as that for the isothermal wall condition.

5 CONCLUSIONS

A three-dimensional numerical procedure was developed to study the friction characteristics for steady laminar incompressible flow in long microchannels. The numerical program was first used to simulate incompressible flow in conventional-size channels subject to isothermal wall boundary conditions. The calculated $f \cdot \mathrm{Re}$ at several different aspect ratios compared quite well with that of the corresponding two-dimensional incompressible fully developed flows calculated by other investigators. This comparison validated our numerical program.

For the isothermal wall condition, the pressure and $f \cdot \mathrm{Re}$ distributions along the channel axis are nonlinear due to the fluid property changes. The $f \cdot \mathrm{Re}$ value reaches a constant for different pressure ratios. This constant equals to that obtained from two-dimensional simulation for constant property fluid. But this constant should not be used for microchannel flows because a large part of the channel deviates from this value.

For the constant heat flux condition, the pressure and $f \cdot \mathrm{Re}$ distributions along the channel axis are also quite nonlinear due to the fluid property changes. Unlike the isothermal wall case, the $f \cdot \mathrm{Re}$ value is different for different heat fluxes. The fluid property changes must be taken into account in analyzing microchannel flows if large temperature variations are involved.

REFERENCES

1. Wu P. Y. and Little W. A., Measurement of Friction Factor for the Flow of Gases in Very Fine Channels Used for Microminiature Joule-Thompson Refrigerators, Cryogenics, Vol.23, pp. 273-7, 1983.
2. Wu P. Y. and Little W. A., Measurement of the Heat Transfer Characteristics of Gas Flow in Fine Channel Heat Exchangers Used for Microminiature Refrigerators, Cryogenics, Vol.24, pp. 415-20, 1984.
3. Choi S. B., Friction Factors and Heat Transfer in Microtube, PhD Thesis, Louisiana Tech University, 1991.
4. Choi S. B., Barron R. F. and Warrington R. O., Fluid Flow and Heat Transfer in Microtubes, Symposium on Micromechanical Sensors, Actuators, and Systems ASME DSC, Vol.32, pp. 123-34, 1991.
5. Yu D., The Effects of The Prandtl Number in Micro Heat Transfer, PhD Thesis, Louisiana Tech University, 1994.
6. Chen C. S., Lee S. M. and Sheu S. D., Numerical Analysis of Gas Flow in Micro-Channels, Numerical Heat Transfer, Part A, Vol.33, pp. 749-62, 1998.
7. Chen C. S. and Kuo W. J., Heat Transfer and Flow Friction for Gaseous Flow in Microtubes, Trans. Aeronautical and Astronautical Society of the Republic of

China, Vol.35, pp. 257-66, 2003.
8. Sobhan C. B. and Garimella S. V., A Comparative Analysis of Studies on Heat Transfer and Fluid Flow in Microchannels, Microscale Thermophysical Eng., Vol.5, pp. 293-311, 2001.
9. Chen, C.S., Numerical Method for Predicting Three-Dimensional Steady Compressible Flow in Long Microchannels, Journal of Micromechanics and Microengineering, Vol.14, No.7, pp. 1091-1100, 2004.
10. Tannehill J. C., Anderson D. A. and Pletcher R. H., Computational Fluid Mechanics and Heat Transfer, Taylor & Francis, 1997.
11. Shah, R.K. and London, A.L., Laminar Flow Forced Convection in Ducts, Academic Press, New York, pp. 196-219, 1978.

Table 1 The simulated conditions for the results of Table 3.

PARAMETER	VALUES
Channel cross sectional area, *AREA*	$1\,cm^2$
Aspect ratio, *AR* （H/W）	1.0、0.75、0.5、0.4、0.25、0.125、0.1
Channel outlet pressure （P_{out}）	$100.8\times10^3 \quad N/m^2$
Pressure ratio , *PR* （P_{in}/P_{out}）	1.001
Fluid temperature at inlet	290K
Isothermal wall temperature	340 *K*

Table 3 The simulated conditions for microchannel flows

PARAMETER	VALUES
Channel cross sectional area, *AREA*	100 μm^2
Aspect ratio, *AR* （H/W）	1.0
Channel outlet pressure （P_{out}）	$100.8\times10^3 \quad N/m^2$
Pressure ratio , *PR* （P_{in}/P_{out}）	2, 4, 6
Fluid temperature at inlet	290K
Isothermal wall temperature	340 *K*
Constant heat flux	12000 ~ 280000 w/m^2

Table 2 The comparison of $f\cdot\mathrm{Re}$ calculated by the present method and [11].

AR	$f\cdot\mathrm{Re}$	2-D Numerical [11]	Errors (%)
1.0	56.8564	56.91	- 0.09
0.75	57.882	57.89	- 0.012
0.5	62.2284	62.19	0.06
0.4	65.4858	65.47	0.02
0.25	72.9643	72.93	0.047
0.125	82.454	82.34	0.14
0.1	84.8353	84.68	0.18

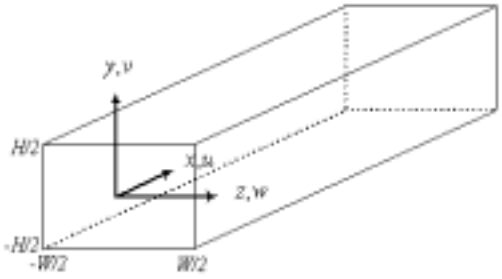

Fig.1 The geometry and coordinate system for the three-dimensional microchannel.

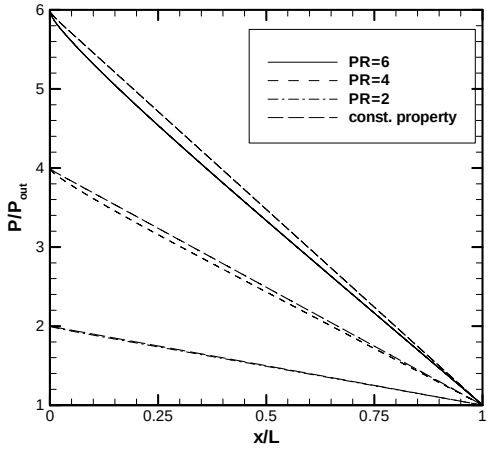

Fig.2 The pressure distributions along the microchannel axis subject to the isothermal wall conditions, PR=2, 4, and 6. The straight constant property line is depicted for comparison.

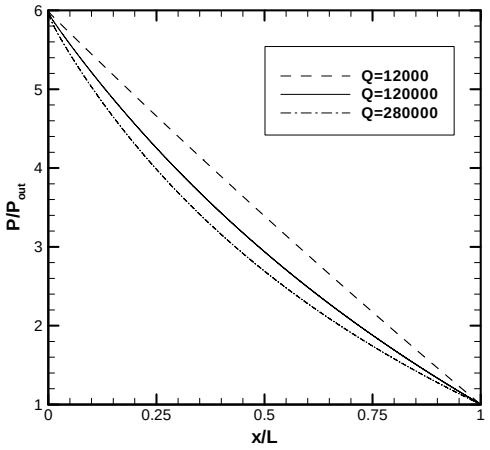

Fig.4 The pressure distributions along the microchannel axis subject to the constant heat flux conditions. The unit for Q is w/m^2 and PR=6.

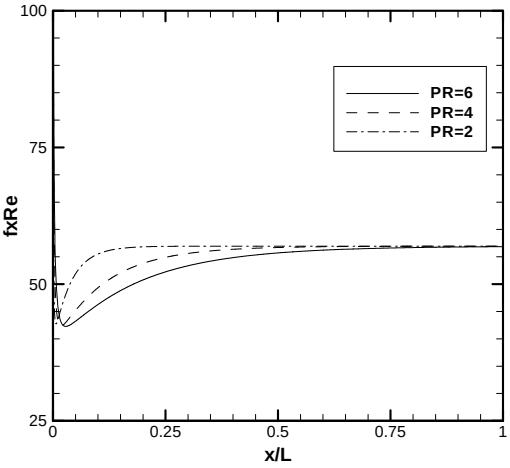

Fig.3 The $f \cdot \mathrm{Re}$ distributions along the microchannel axis subject to the isothermal wall conditions, PR=2, 4, and 6.

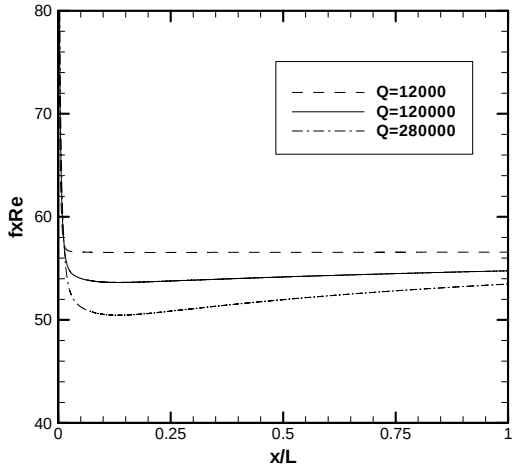

Fig.5 The $f \cdot \mathrm{Re}$ distributions along the microchannel axis subject to the constant heat flux conditions. The unit for Q is w/m^2 and PR=6.